

- length, and dynamic collective pinning effects), and a quantitative comparison between transport and neutron results will have to await further neutron measurements at elevated temperatures.
13. V. G. Kogan and L. J. Campbell, *Phys. Rev. Lett.* **62**, 1552 (1989); L. J. Campbell, M. M. Doria, V. G. Kogan, *Phys. Rev. B* **38**, 2439 (1988).
  14. G. Blatter and V. Geshkenbein, *Phys. Rev. B* **47**, 2725 (1993).
  15. Specifically, the deformed lattice corresponding to Eq. 2 can be approximately obtained from Eq. 1 by two orthogonal shear deformations,  $\hat{u}_1 = \mu_1 y \hat{z}$  and  $\hat{u}_2 = \mu_2 z \hat{y}$ . The shear deformation  $\hat{u}_1$  (with  $\mu_1 = \sin 15^\circ / \cos \theta \epsilon(\theta)$  for  $\chi = 0^\circ$  and  $\phi = 45^\circ$ ) vanishes between  $\theta = 70^\circ$  and  $\theta = 80^\circ$ . The modulus for this shear mode (13) is  $c_{66} = \Phi_0 B \epsilon^3(\theta) / (64\pi^2 \lambda_{ab}^2)$ , where  $\lambda_{ab}$  is the penetration depth in the  $ab$  plane. The elastic energy  $c_{66}(\mu_1/2)^2$  thus increases with  $\theta$  as  $\epsilon^2(\theta)/\cos(\theta)$ , so that it is weakly dependent on  $\theta$  for angles  $\leq 70^\circ$ , but increases sharply for a larger  $\theta$ . This increase inevitably causes a reorientation in this range of angles. Clearly, the sharp reorientation implied in this argument is an artifact of the two-dimensional approximation we used in deriving Eq. 2. A refined model would smoothly interpolate between Eq. 1 and Eq. 2, as experimentally observed in our diffraction pattern for  $\theta = 70^\circ$ . A crude estimate of the pinning energy per pancake (or stack of pancakes) can be obtained from the morphology change we observe at  $\alpha_c \sim 30^\circ$  ( $\theta \sim 45^\circ$ ). On the assumption that for  $\alpha < \alpha_c$  the vortices "kink" into

- segments of length  $\sim D \cos \alpha$  pinned by the twin planes and unpinned sections of length  $\sim D \sin \alpha$ , and because the vortex line tension is  $E_0 \epsilon(\theta) \ln[\lambda_{ab}/\xi \epsilon(\theta)]$ , with  $E_0 = \Phi_0 / 16\pi^2 \lambda_{ab}^2$  [R. A. Klemm and J. R. Clem, *Phys. Rev. B* **21**, 1868 (1980)], vortex bending becomes energetically unfavorable for  $\tan \alpha_c \approx V_p / E_0$ , where  $V_p$  is the pinning energy per unit length (logarithmic corrections of order unity depend on the detailed path taken by the vortices). According to the scenario discussed in the text, we expect  $V_p$  to be reduced by a factor  $\sim d/D$  for  $\alpha > \alpha_c$ . Equating this relation to the elastic energy for the shear mode  $\hat{u}_1$  yields  $\theta \approx 80^\circ$  for the reorientation angle, consistent with our measurement.
16. G. J. Dolan, F. Holtzberg, C. Feild, T. R. Dinger, *Phys. Rev. Lett.* **62**, 2184 (1989).
  17. P. L. Gammel *et al.*, *ibid.* **68**, 3343 (1992).
  18. B. I. Ivlev and N. B. Kopnin, *Phys. Rev. B* **44**, 2747 (1991); ———, M. M. Salomaa, *ibid.* **43**, 2896 (1991).
  19. We thank J. Barker and C. Glinka for help with the small-angle neutron scattering instrument and software; V. Kiryukhin for assistance with the experiment; and D. J. Bishop, V. G. Kogan, and N. P. Ong for helpful discussions. Supported by the Advanced Research Projects Agency and the Air Force Office of Scientific Research (AFOSR) under grants AFOSR No. F49620-90-C-0079 and No. F49620-93-1-0259.

10 June 1993; accepted 11 August 1993

## Anatomy of the Photodissociation Region in the Orion Bar

A. G. G. M. Tielens, M. M. Meixner, P. P. van der Werf, J. Bregman, J. A. Tauber, J. Stutzki, D. Rank

Much of the interstellar gas resides in photodissociation regions whose chemistry and energy balance is controlled by the flux of far-ultraviolet radiation upon them. These photons can ionize and dissociate molecules and heat the gas through the photoelectric effect working on dust grains. These regions have been extensively modeled theoretically, but detailed observational studies are few. Mapping of the prominent Orion Bar photodissociation region at wavelengths corresponding to the carbon-hydrogen stretching mode of polycyclic aromatic hydrocarbons, the 1-0 S(1) line of molecular hydrogen, and the  $J = 1-0$  rotational line of carbon monoxide allows the penetration of the far-ultraviolet radiation into the cloud to be traced. The results strongly support the theoretical models and show conclusively that the incident far-ultraviolet radiation field, not shocks as has sometimes been proposed, is responsible for the emission in the Orion Bar.

Photodissociation regions (PDRs), sometimes called photodominated regions, are regions in which far-ultraviolet (FUV) photons with energies less than the hydrogen ionization limit dominate the energy bal-

ance or chemical composition of the interstellar gas (1). PDRs are associated with HII regions, reflection nebulae, bright-rim clouds, planetary nebulae, and normal and active galactic nuclei (2). Indeed, most of the neutral atomic and molecular gas in the galaxy is in regions where penetrating FUV photons play an important role.

Although much theoretical effort has been expended on the development of models for the interaction of FUV photons with interstellar gas, little direct observational data on this interaction is presently available. Photons with energies above 13.6 eV can ionize H and, in a natural way, lead to ionized gas regions with temperatures of  $10^4$  K, which emit predominantly in the visible and UV. Hence, observation-

al studies of  $H^+$  regions have a long and distinguished history in astronomy. In contrast, neutral atomic and molecular gas cool down to much lower temperatures ( $< 10^3$  K) and in consequence emit essentially all of their energy at infrared (IR) and submillimeter wavelengths. Because of the high thermal background associated with ground-based telescopes, observations in the IR require special techniques, and very extended regions of low surface brightness (which encompass most of the galactic gas) are impossible to study.

We circumvented this problem by studying a dense and compact region near a luminous O star, which hence has a high surface brightness. Recent advances in IR detector technology now allow efficient mapping of such objects in the rovibrational lines of  $H_2$  and the vibrational transitions of polycyclic aromatic hydrocarbon molecules (PAHs). Moreover, present telescope arrays operating at millimeter wavelength can spatially resolve these regions in the transition of the most abundant carbon-bearing molecule, CO. Hence, a combination of these techniques permits a direct observational study of the detailed interaction of FUV photons with atomic and molecular gas.

Theoretical studies (1) show that for a bright PDR, as considered here, the chemical structure is mainly determined by the penetration of FUV photons and hence by the dust extinction. A nearby O star creates a surface layer of predominantly neutral gas (mostly neutral H along with neutral O and  $C^+$  and  $Si^+$ ) that separates the ionized gas from the surrounding prenatal molecular cloud. At an optical depth of about  $A_v = 2$  magnitudes (mag), the dissociating photons have been sufficiently attenuated, and neutral H transforms into  $H_2$ . Similarly, at  $A_v \approx 4$  mag, the carbon balance shifts from  $C^+$  to neutral C and CO.

The penetrating FUV photons also dominate the energy balance of the gas. Near the surface ( $A_v < 4$  mag), heating occurs primarily through the photoelectric effect on dust grains and PAH molecules. The gas cools predominantly through atomic fine-structure lines: notably, [OI] 63  $\mu m$  and [CII] 158  $\mu m$  (neutral O and singly ionized C, which have lines at wavelengths,  $\lambda$ , of 63 and 158  $\mu m$ , respectively; the brackets indicate a "forbidden" transition). The gas in this zone is fairly warm,  $\approx 500$  K, much warmer than the dust ( $\approx 75$  K). Because of dust attenuation, photoelectric heating becomes less important deeper in the PDR ( $A_v > 4$  mag), and collisions of gas species with warm dust grains, heated by penetrating visible and IR photons, take over as the dominant heating source. The gas cools efficiently through CO rotational lines. As a result, the gas is now slightly cooler ( $\approx 50$

A. G. G. M. Tielens and J. Bregman, MS 245-3 NASA Ames Research Center, Moffett Field, CA 94035-1000.

M. M. Meixner, Radioastronomy Laboratory, University of California, Berkeley, CA 94720.

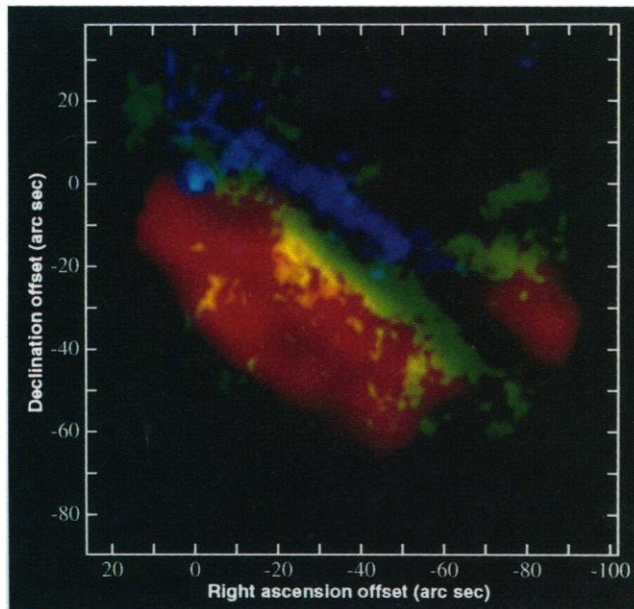
P. P. van der Werf, Max Planck Institut für Extraterrestrische Physik, Giessenbach Strasse, D-8046 Garching bei München, Germany.

J. A. Tauber, Radioastronomy Laboratory, University of California, Berkeley, CA 94720, and ESA Astrophysics Division, ESTEC, P.O. Box 299, NL-2200 AG Noordwijk, the Netherlands.

J. Stutzki, I. Physikalisches Institut, Universität Köln, Zùlpicherstrasse 77, W-5000 Köln 41, Germany.

D. Rank, Lick Observatories, University of California, Santa Cruz, CA 95060.

**Fig. 1.** False color picture of the PDR in the Orion Bar. Blue is emission in the 3.3- $\mu\text{m}$  PAH emission feature (30). Green is emission in the 1-0 S(1)  $\text{H}_2$  line at 2.122  $\mu\text{m}$  (31). Red is emission in the CO 1-0 transition (32). For the near-IR maps (PAH and  $\text{H}_2$ ), absolute registration was determined from the pixel size and the position of the (unrelated) star  $\theta^2\text{A Ori}$  (1950 coordinates:  $5^{\text{h}} 32^{\text{m}} 55.4^{\text{s}}$ ,  $5^{\circ} 26' 50.7''$ ) present in both images [at the (0,0) position]. There is essentially no continuum at these wavelengths (33). The exciting star,  $\theta^1\text{C Ori}$ , and the ionized gas are located to the northwest. For all three molecular tracers, the emission is concentrated in a bar parallel to but displaced toward the southeast of the ionization front. The FUV ( $h\nu < 13.6$  eV) photons from the ionizing star penetrate the atomic and molecular cloud and photodissociate, photoionize, and heat the gas. Each of these molecular tracers interacts differently with the radiation field, and hence, this comparison allows us to study the penetration of FUV photons.



K) than the dust. We compare these theoretical predictions with observations of the PDR associated with the prominent ionization front to the southeast of the Orion HII region, the Orion Bar.

The ionizing star,  $\theta^1\text{C Ori}$ , has created an optically bright, bowl-shaped HII region on the surface of the Orion molecular cloud (3). The Orion Bar is the limb-brightened edge of this bowl where an ionization front is eating its way into the molecular cloud. Optically, the HII region shows a sharp edge to the southeast. The bar itself is particularly prominent in the radio (free-free) and in the [OI]  $\lambda 6300 \text{ \AA}$  and [SII]  $\lambda 6731 \text{ \AA}$  lines (4, 5). The IR and millimeter emission studied here is located to the southeast of the optical and radio emission (Fig. 1). Each of the different tracers shows a relatively narrow emission zone parallel to but offset from (to the southeast of) the free-free emission (6). The 3.3- $\mu\text{m}$  PAH emission feature coincides with emission in the [SII]  $\lambda 6731 \text{ \AA}$  (5), which traces the front surface of the PDR (7). The peak in the  $\text{H}_2$  emission is displaced further into the molecular cloud by about 10 arc sec, whereas the CO emission peaks about 20 arc sec deeper into the molecular cloud (Fig. 1). Maps of this region at 609  $\mu\text{m}$  ([CI]) reveal a similar narrow, barlike structure coincident with the CO bar in our data (8).

The observations of the Orion Bar are typical for an edge-on PDR. The 3.3- $\mu\text{m}$  emission feature and the associated features at 6.2, 7.7, and 11.3  $\mu\text{m}$  are very characteristic of PAH materials either in gaseous or solid form (9). The observed high exci-

tation in the Orion Bar far from the illuminating star implicates, however, a molecular carrier with typically 50 C atoms (9, 10). Because PAH molecules (or solids for that matter) are very stable against photodissociation in atomic zones, the observed 3.3- $\mu\text{m}$  intensity traces the attenuation of the pumping FUV photons. In contrast,  $\text{H}_2$  and CO are very susceptible to photodissociation, and their emission zones will be displaced into the cloud by 2 and 4 magnitudes of visible extinction, respectively.

Hence, the separation between the emission peaks of the different tracers measures directly the FUV penetration size scale. Adopting a hydrogen column density,  $N$ , per magnitude of visual extinction,  $N_{\text{H}}/A_v = 1.9 \times 10^{21} \text{ cm}^{-2} \text{ mag}^{-1}$  (11) and a distance of 500 pc, the observed scale size of the region (5 arc sec per magnitude of visual extinction) implies a gas density of  $5 \times 10^4 \text{ cm}^{-3}$  for a homogenous region viewed edge-on. A viewing angle of  $45^\circ$  would change this density estimate to  $10^4 \text{ cm}^{-3}$  (12). Figure 2 compares observational cross cuts across the Orion Bar in the PAH,  $\text{H}_2$ , and CO lines with detailed PDR model calculations for a homogenous slab of density  $5 \times 10^4 \text{ cm}^{-3}$  faced edge-on (line-of-sight extent 0.12 pc) (13). Given a density and incident FUV field (14), these models calculate the energy balance, chemical composition, and radiative transfer in the FUV and the cooling lines self consistently (1). Details of these model calculations will be described elsewhere (12). Here, we point out that the observed and calculated

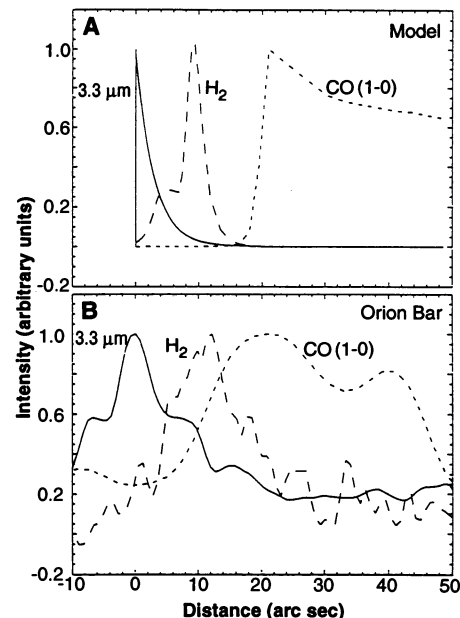


**Fig. 2.** Comparison between (A) calculated and (B) observed cross cuts through the Orion Bar. The observed cross cut was taken through the center of the map ( $-38.9$  arc sec,  $-24.5$  arc sec) at a position angle of  $45^\circ$  (perpendicular to the bar). The calculated intensities (12) have not been convolved with beam profiles. The observed separation between the emission peaks is mainly sensitive to the FUV dust absorption column density. For standard dust parameters, a good match is obtained for a density of  $5 \times 10^4 \text{ cm}^{-3}$ .

emission scale size are in excellent agreement for this density. Calculated absolute intensities also agree reasonably well with the observations (12).

The inferred density of  $5 \times 10^4 \text{ cm}^{-3}$  agrees well with independent estimates of the density in the Orion Bar. The ionized gas in the Orion Bar region has an estimated density of  $6 \times 10^3 \text{ cm}^{-3}$  (15). If we assume pressure equilibrium across the ionization front, this estimate requires a neutral gas density of  $10^5 \text{ cm}^{-3}$  for a temperature of 1000 K. Molecular observations (of CS, HCN, and CO) also reveal densities in the range  $10^4$  to  $10^5 \text{ cm}^{-3}$  in the Orion Bar (12, 16). Because PDRs are generally clumpy (17), this can affect the penetration of FUV radiation into a region considerably (18). However, theoretical studies (12) show that the clumps present in the CO map have little influence on the FUV penetration into the Orion Bar because of their low volume-filling factor. In contrast, on the much larger scale of the whole Orion nebula ( $\approx 10$  arc min), the clumpy and filamentary structure of the molecular cloud dominates the PDR emission scale size (19). We note also that a high-density clump component is required to explain some of the observed emission characteristics of the Orion Bar, including bright, high-level CO emission and some  $\text{H}_2$  line ratios.

**Table 1.** Observations and models of the Orion Bar.

Species	Wavelength ( $\mu\text{m}$ )	Beam (arc sec)	Intensity ( $\text{erg cm}^{-2} \text{s}^{-2} \text{sr}^{-1}$ )		Reference
			Observed	Model*	
Neutral O	63	45	$4 \times 10^{-2}$	$7 \times 10^{-2}$	(19)
Neutral O	146	45	$2 \times 10^{-3}$	$5 \times 10^{-3}$	(19)
C <sup>+</sup>	158	45	$6 \times 10^{-3}$	$7 \times 10^{-3}$	(19)
Si <sup>+</sup>	35	47	$9 \times 10^{-3}$	$2 \times 10^{-2}$	(34)
Neutral C	609	15	$5 \times 10^{-6}$	$6 \times 10^{-6}$	(8)
Neutral C	370			$4 \times 10^{-5}$	
CO 1-0	2600	7	$4 \times 10^{-7}$	$2 \times 10^{-7}$	(12)
CO 7-6	373	26	$2 \times 10^{-4}$	$3 \times 10^{-4\dagger}$	(19)
CO 14-13	186	60	$3 \times 10^{-4}$	$1 \times 10^{-4\dagger}$	(19)

\*Calculated (12) peak intensities for a homogeneous PDR with a density of  $5 \times 10^4 \text{ cm}^{-3}$ . †For a clump with a density of  $10^7 \text{ cm}^{-3}$  at the PDR surface; the homogeneous model produces negligible emission in these lines (12).

Atomic fine-structure lines of C<sup>+</sup>, Si<sup>+</sup>, and neutral O are sensitive to the density and temperature of the neutral gas in the PDR (1). Model results (12) and observations compare well (Table 1), further supporting the density derived from the observed spatial structure. Finally, the calculated gas temperature at the surface of the PDR (500 to 1000 K) is also in good agreement with the temperature derived directly from the observed pure rotational lines of H<sub>2</sub> (20).

In the past, emission in the Orion Bar region has often been interpreted in terms of a weak shock driven by the expanding HII region (21). The observed velocity difference between the bar region and the Orion Ridge ( $2 \text{ km s}^{-1}$ ) is then cited as support for such a dynamic interaction. However, both the CO and the H<sub>2</sub> bars are centered at  $10 \text{ km s}^{-1}$  (12, 22), and hence, any shock present must have propagated well beyond the CO emission evident in our map and therefore does not contribute to the excitation in this region anymore. Moreover, in a shock interpretation, the H<sub>2</sub> emission should originate in warm gas closer to the shock front, or deeper in the cloud, than the cooler gas responsible for CO emission, which is just the opposite of the observed morphology.

Finally, a weak shock driven by an expanding HII region would not produce much emission in the H<sub>2</sub> lines (23). The total mechanical energy input ( $\rho_0 v^3/2$ , where  $\rho_0$  and  $v$  are the preshock density and shock velocity) by a  $3 \text{ km s}^{-1}$  shock into gas with density of  $5 \times 10^4 \text{ cm}^{-3}$  is  $\approx 10^{-3} \text{ erg cm}^{-2} \text{ s}^{-1}$  or only  $\approx 10^{-5}$  of the FUV field incident on the Orion Bar ( $65 \text{ erg cm}^{-2} \text{ s}^{-1}$ ). The total H<sub>2</sub> emission shock velocity from such a shock is calculated to be less than  $10^{-3}$  of this mechanical energy (23). This conversion efficiency is somewhat better than that of FUV-pumped IR fluorescence [ $5 \times 10^{-4}$  for these conditions (24)]. Nevertheless, any emission from shocked H<sub>2</sub> gas is dwarfed

by fluorescence unless the shock velocity is well in excess of  $10 \text{ km s}^{-1}$ . Such a high shock velocity is, however, not expected for an evolved HII blister-like Orion because this would require a dynamical age less than  $10^3$  years.

The high ratio of the intensities of the 1-0 S(1) and 2-1 S(1) H<sub>2</sub> lines observed in the Orion Bar region (25) indicates a substantial contribution to the 1-0 S(1) emission by warm gas. This has often been taken as evidence for a contribution by shocks to the H<sub>2</sub> emission. However, in view of the arguments presented above, we ascribe this emission to warm gas associated with PDRs on the surface of dense ( $10^7 \text{ cm}^{-3}$ ) clumps. Dense clumps have a thin surface layer of warm (2000 K) molecular gas, which, like shocks, emits preferentially in the 1-0 transitions of H<sub>2</sub>. Indeed, models of dense PDRs are in good agreement with the observed H<sub>2</sub> intensity ratio (26). Furthermore, the H<sub>2</sub> map shows evidence for small-scale clumping. There is independent evidence for the presence of dense clumps in the Orion Bar region in our CO and CS maps (12, 27). The observed high intensity of the CO 14-13 line in the Orion Bar (19) also attests to the presence of warm ( $>500 \text{ K}$ ), dense ( $>10^7 \text{ cm}^{-3}$ ) molecular gas, again in good agreement with model calculations of dense PDRs (25).

We have studied the PDR in the Orion Bar in various molecular tracers. In this way, we have been able to probe the detailed interaction of penetrating FUV photons with atomic and molecular gas. The observations are in very good agreement with theoretical predictions and hence strongly support current theoretical models for this interaction. Such models have been applied to observations of reflection nebulae, planetary nebulae (28), the galactic center, and the nuclei of starburst galaxies. Similar observations of these types of objects can further elucidate the interaction of FUV photons with interstellar dust and gas. Moreover, it can test present models for the

heating and cooling and detailed chemistry of the general interstellar medium.

## REFERENCES AND NOTES

1. A. G. G. M. Tielens and D. J. Hollenbach, *Astrophys. J.* **291**, 722 (1985).
2. For a review, see R. Genzel, A. I. Harris, J. Stutzki, in *IR Spectroscopy and Astronomy*, B. H. Kaldeich, Ed. (European Space Agency, SP-290, Paris, 1989), p. 115.
3. B. Zuckerman, *Astrophys. J.* **183**, 863 (1973).
4. G. Garay, J. M. Moran, M. J. Reid, *ibid.* **314**, 535 (1987); T. R. Gull, in *HII Regions and The Galactic Centre*, A. F. M. Moorwood, Ed. (European Space Research Organization, SP-105, Paris, 1974), p. 1.
5. R. W. Pogge, J. M. Owen, B. Atwood, *Astrophys. J.* **399**, 147 (1992).
6. D. K. Aitken, P. F. Roche, P. M. Spencer, B. Jones, *Astron. Astrophys.* **76**, 60 (1979); M. Burton, A. Moorhouse, P. W. J. L. Brand, P. F. Roche, T. R. Geballe, in *Interstellar Dust: Contributed Papers* A. G. G. M. Tielens and L. J. Allamandola, Eds., (National Aeronautics and Space Administration, SP-3036, Washington, DC, 1987).
7. J. F. Hester, *Publ. Astron. Soc. Pac.* **103**, 853 (1991).
8. G. J. White and R. Padman, *Nature* **354**, 511 (1991); J. Tauber, D. Lis, T. Buettgenbach, J. Keene, in preparation.
9. L. J. Allamandola, A. G. G. M. Tielens, J. R. Barker, *Astrophys. J. Suppl. Ser.* **71**, 733 (1989); W. W. Duley, in *Interstellar Dust*, L. J. Allamandola and A. G. G. M. Tielens, Eds. (Kluwer, Dordrecht, Netherlands, 1989), p. 141.
10. A. G. G. M. Tielens in *Dust and Chemistry in Astronomy*, T. J. Millar and D. A. Williams, Eds. (Institute of Physics, Bristol, UK, 1993), p. 103. For an opposing view, see W. W. Duley and D. A. Williams, *Mon. Not. R. Astron. Soc.* **231**, 969 (1988).
11. R. C. Bohlin, B. D. Savage, J. F. Drake, *Astrophys. J.* **224**, 132 (1978).
12. J. A. Tauber, M. Meixner, A. G. G. M. Tielens, P. F. Goldsmith, *ibid.*, in press.
13. M. W. Werner *et al.*, *ibid.* **204**, 420 (1976).
14. A field  $5 \times 10^4$  times the average interstellar radiation field. A. G. G. M. Tielens and D. J. Hollenbach, *ibid.* **291**, 747 (1985).
15. A. H. M. Martin and S. F. Gull, *Mon. Not. R. Astron. Soc.* **175**, 235 (1976); J. P. Simpson, R. H. Simpson, E. F. Erickson, M. Haas, *Astrophys. J.* **311**, 895 (1986).
16. T. Omodaka, M. Hayashi, T. Hasegawa, *Astrophys. J.* **282**, L77 (1984).
17. J. Stutzki *et al.*, *Astrophys. J.* **332**, 379 (1988); J. Stutzki and R. Gusten, *ibid.* **356**, 513 (1990); M. Meixner, M. R. Haas, A. G. G. M. Tielens, E. F. Erickson, M. W. Werner, *ibid.* **390**, 499 (1992).
18. P. Boisse, *Astron. Astrophys.* **228**, 483 (1990).
19. G. J. Stacey *et al.*, *Astrophys. J.* **404**, 219 (1993).
20. S. P. Parnmar, J. H. Lacy, J. Achtermann, *Astrophys. J.* **372**, L25 (1991).
21. F. P. Schloerb and R. B. Loren, in "Symposium on the Orion Nebula to honor Henry Draper", *Ann. N.Y. Acad. Sci.* **395**, 32 (1982).
22. I. Gatley and N. Kaifu, in *Astrochemistry*, M. S. Vardya and S. P. Tarafdar, Eds. (Reidel, Dordrecht, Netherlands, 1987), p. 153.
23. B. T. Draine, W. G. Roberge, A. Dalgarno, *Astrophys. J.* **264**, 485 (1983).
24. J. H. Black and E. F. van Dishoeck, *ibid.* **322**, 412 (1987).
25. M. Hayashi, T. Hasegawa, I. Gatley, R. Garden, N. Kaifu, *Mon. Not. R. Astron. Soc.* **215**, 31P (1985).
26. A. Sternberg and A. Dalgarno, *Astrophys. J.* **347**, 863 (1989); M. G. Burton, D. J. Hollenbach, A. G. G. M. Tielens, *ibid.* **365**, 620 (1990).
27. P. P. van der Werf, J. Stutzki, A. Sternberg, R. Genzel, in preparation.
28. J. R. Graham *et al.*, *Astron. J.* **105**, 250 (1993).
29. J. Bregman *et al.*, in preparation.
30. Acquired with the Lick-Ames near-IR camera at the National Aeronautics and Space Administration's Mount Lemmon telescope (29). In Sb array,

- 128 by 128; pixel size, 0.75 arc sec; effective resolution, 2 arc sec.
31. Observed with the FAST camera on the European South Observatory–Max Planck Institute 2.2-m telescope at La Silla, Chile (27). In Sb array, 62 by 58; pixel size, 0.78 arc sec; effective resolution, 2 arc sec.
32. Obtained with the Hat Creek interferometer (12). Effective resolution, 7.5 arc sec. The absolute

- position of these maps is accurate to 0.15 arc sec.
33. T. R. Geballe, A. G. G. M. Tielens, L. J. Allamandola, A. Moorhouse, P. W. J. L. Brand, *Astrophys. J.* 341, 278 (1989).
34. M. Haas, D. Hollenbach, E. F. Erickson, *Astrophys. J.* 301, L57 (1986).

7 June 1993; accepted 2 August 1993

## Protein Ladder Sequencing

Brian T. Chait, Rong Wang, Ronald C. Beavis, Stephen B. H. Kent\*

A new approach to protein sequencing is described. It consists of two steps: (i) ladder-generating chemistry, the controlled generation from a polypeptide chain by wet chemistry of a family of sequence-defining peptide fragments, each differing from the next by one amino acid; and (ii) data readout, a one-step readout of the resulting protein sequencing ladder by matrix-assisted laser-desorption mass spectrometry. Each amino acid was identified from the mass difference between successive peaks, and the position in the data set defined the sequence of the original peptide chain. This method was used to directly locate a phosphoserine residue in a phosphopeptide. The protein ladder sequencing method lends itself to very high sample throughput at very low per cycle cost.

Direct experimental determination of the amino acid sequence of a polypeptide chain usually gives partial sequence data only. Partial amino acid sequence data may be used to identify isolated proteins (1), and are useful in cloning genes (2). The complete amino acid sequence of a protein is most often determined by nucleic acid sequencing at the cDNA level. However, posttranslational modifications (3) must be characterized at the polypeptide level.

Most direct sequence determination of peptides and proteins is done by automated Edman degradation (4), in which a two-part chemical reaction is used to remove one amino acid at a time from the amino terminal. After release, each amino acid derivative is converted to a stable form and is then identified by analytical reverse-phase high-performance liquid chromatography. Currently such sequencing is limited to less than ~50 residues per day (5). Also, most posttranslational modifications are not identified. Thus, there is a great need for more rapid and versatile protein sequencing methods (6).

The recent advent of matrix-assisted laser-desorption mass spectrometry (LDMS) (7) and the development of improved matrix materials (8) has facilitated the accurate measurement of the mass of intact

polypeptide chains. Subpicomole amounts of total sample can be analyzed in seconds with a mass accuracy of up to 1 part in 10,000 (9). Thus the polypeptide itself can be analyzed more readily, with greater speed, sensitivity, and precision, than the amino acid derivative released by stepwise sequencing (10).

We describe a new principle in protein sequencing that combines multiple steps of wet degradation chemistry with a final, single-step mass spectrometric (MS) readout of the amino acid sequence. First, a sequence-defining concatenated set of peptide fragments, each differing from the next by a single residue, is chemically generated in a controlled fashion. Second, matrix-assisted LDMS is used to read out the complete fragment set in a single operation, as a "protein sequencing ladder" data set.

A concatenated set of peptide fragments can be generated in a controlled fashion (11) by carrying out rapid stepwise degradation in the presence of a small amount of terminating agent, a procedure we call "ladder-generating chemistry" (Fig. 1). A small proportion of peptide chain blocked at the amino terminus is generated at each cycle. A predetermined number of cycles is performed without intermediate separation or analysis of the released amino acid derivatives. The resulting mixture is read out in a single operation by matrix-assisted LDMS (12). The mass spectrum contains molecule ions corresponding to each terminated polypeptide species present. The mass differences between consecutive peaks each correspond to an amino acid residue (13), and their order of occurrence in the data set defines

the sequence of amino acids in the original peptide chain (14).

We sequenced the 14-residue peptide [Glu<sup>1</sup>]fibrinopeptide B (15) to illustrate the new method. Eight cycles of manual ladder-generating chemistry were carried out (16), and the resulting product mixture of terminated peptides read out (17) by matrix-assisted LDMS (Fig. 2). All the major components present in the mass spectrum were readily identified, and the data could be simply interpreted to give the sequence of the eight amino-terminal residues of the peptide. The two consecutive peaks with the highest mass differ by 129.1 daltons, identifying the amino-terminal amino acid as a Glu residue (calculated residue mass 129.1). The identities of the next seven residues were read off in a similar fashion (18).

Several features of the protein ladder sequencing experiment are immediately apparent. The mass accuracy obtained (9) was sufficient to unambiguously distinguish Asp [calculated residue mass 115.1] (13) and Asn (calculated residue mass 114.1); Glu [calculated residue mass 129.1] was also identified with sufficient accuracy to distinguish it from Gln [calculated residue mass 128.1]. The arbitrary ratio of degradation-to-terminating reagents and the minimal

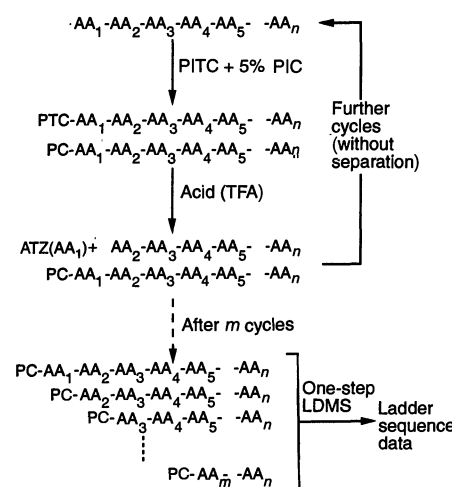


Fig. 1. Protein ladder sequencing principle exemplified by the generation of a set of sequence-determining fragments from an intact peptide chain with controlled ladder-generating chemistry. A stepwise degradation (32) is carried out with a small amount of terminating agent present in the coupling step. In this case, 5% phenylisocyanate (PIC) was added to the phenylisothiocyanate (PITC). The phenylcarbamyl (PC) peptides formed are stable to the trifluoroacetic acid (TFA) used to cyclize and cleave the terminal amino acid (AA) from the phenylthiocarbonyl (PTC) peptide. Successive cycles of ladder-generating chemistry are performed without intermediate isolation or analysis of released amino acid derivatives. Finally, the mixture of PC peptides is read out in one step by matrix-assisted LDMS.

B. T. Chait and R. Wang, The Rockefeller University, New York, NY 10021.

R. C. Beavis, Department of Physics, Memorial University of Newfoundland, St. John's, Newfoundland, Canada A1B 3X7.

S. B. H. Kent, The Scripps Research Institute, La Jolla, CA 92037.

\*To whom correspondence should be addressed.